Acoustic radiation- and streaming-induced microparticle velocities determined by microparticle image velocimetry in an ultrasound symmetry plane

Rune Barnkob,[1,*] Per Augustsson,[2] Thomas Laurell,[2,3] and Henrik Bruus[4]

[1]*Department of Micro- and Nanotechnology, Technical University of Denmark, DTU Nanotech Building 345 East, DK-2800 Kongens Lyngby, Denmark*

[2]*Department of Measurement Technology and Industrial Electrical Engineering, Division of Nanobiotechnology, Lund University, Box 118, S-221 00 Lund, Sweden*

[3]*Department of Biomedical Engineering, Dongguk University, Seoul, South Korea*

[4]*Department of Physics, Technical University of Denmark, DTU Physics Building 309, DK-2800 Kongens Lyngby, Denmark*

(Received 31 August 2012; published 13 November 2012)

We present microparticle image velocimetry measurements of suspended microparticles of diameters from 0.6 to 10 μm undergoing acoustophoresis in an ultrasound symmetry plane in a microchannel. The motion of the smallest particles is dominated by the Stokes drag from the induced acoustic streaming flow, while the motion of the largest particles is dominated by the acoustic radiation force. For all particle sizes we predict theoretically how much of the particle velocity is due to radiation and streaming, respectively. These predictions include corrections for particle-wall interactions and ultrasonic thermoviscous effects and match our measurements within the experimental uncertainty. Finally, we predict theoretically and confirm experimentally that the ratio between the acoustic radiation- and streaming-induced particle velocities is proportional to the actuation frequency, the acoustic contrast factor, and the square of the particle size, while it is inversely proportional to the kinematic viscosity.

DOI: 10.1103/PhysRevE.86.056307 PACS number(s): 47.15.−x, 43.25.Nm, 43.25.Qp, 43.20.Ks

I. INTRODUCTION

Acoustofluidics, i.e., ultrasound handling of fluids and particle suspensions, recently reviewed in Refs. [1,2], is a field in rapid growth for its use in biological applications such as separation and manipulation of cells and bioparticles. Microchannel acoustophoresis has largely been limited to manipulation of micrometer-sized particles such as yeast [3], blood cells [4], cancer cells [5–7], natural killer cells [8], and affinity ligand complexed microbeads [9], for which the acoustic radiation force dominates. Precise acoustic control of submicrometer particles (e.g., small bacteria, vira, and large biomolecules) remains a challenge due to induction of acoustic streaming of the suspending fluid. Nevertheless, acoustic streaming has been used to enhance the convective transport of substrate in a microenzyme reactor for improved efficiency [10], while acoustic manipulation of submicrometer particles has been achieved in a few specific cases including enhanced biosensor readout of bacteria [11] and bacterial spores [12] and trapping of *E. coli* bacteria [13].

When a standing ultrasound wave is imposed in a microchannel containing an aqueous suspension of particles, two forces of acoustic origin act on the particles: the Stokes drag force from the induced acoustic streaming and the acoustic radiation force from sound wave scattering on the particles. To date, the experimental work on acoustophoresis has primarily dealt with cases where the acoustic radiation force dominates the motion, typically for particles of diameters larger than 2 μm. Quantitative experiments of 5-μm-diam polymer particles in water [14–16] have shown good agreement with the classical theoretical predictions [17,18] of the acoustic radiation force acting on a microparticle of radius a much smaller than the acoustic wavelength λ, where the viscosity of the suspending fluid is neglected. However, as the particle diameter decreases below 2 μm, a few times the acoustic boundary-layer thickness, the particle motion is typically strongly influenced by the Stokes drag force from the induced acoustic streaming flow, which has been reported by several groups [19–21], and the radiation force is modified due to the acoustic boundary layer [22].

As pointed out in a recent review [19], the acoustic streaming is difficult to fully characterize due to its many driving mechanisms and forms. In acoustofluidic systems, the streaming is primarily boundary driven, arising at rigid walls from the large viscous stresses inside the submicrometer-thin acoustic boundary layer of width δ. The boundary-driven acoustic streaming was treated theoretically by Rayleigh [23] for an isothermal fluid in an infinite parallel-plate channel with a standing wave parallel to the plates of wavelength λ much larger than the plate distance h, where h is large compared to δ, i.e., $\lambda \gg h \gg \delta$. However, in many applications of acoustofluidic systems the channels provide enhanced confinement, the acoustic wavelength is comparable to the channel height, and the liquid cannot be treated as being isothermal. Rayleigh's prediction is often cited, but the literature is lacking a quantitative validation of its accuracy when applied to acoustofludic systems. This lack of quantitative tests is most likely due to the fact that boundary-driven acoustic streaming is very sensitive to geometry and boundary conditions, making it difficult to achieve sufficient experimental control. However, quantitative comparisons between theory and experiment of acoustic streaming are crucial for the advancement of the acoustofluidics research field. Understanding and controlling the ratio of radiation- and streaming-induced acoustophoretic velocities may be the key for future realization of ultrasound manipulation of submicrometer particles.

*Corresponding author: barnkob@alumni.dtu.dk

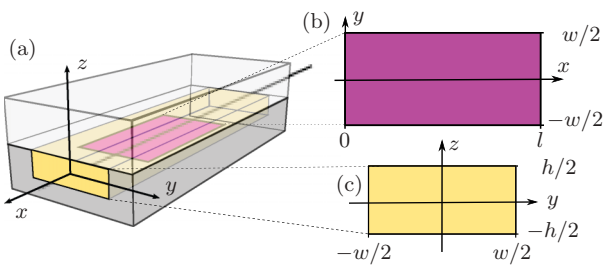

FIG. 1. (Color online) (a) Sketch of the silicon and glass microchip used in our experiments (see also Ref. [14]). It contains a straight rectangular water-filled microchannel of length $L = 35$ mm, width $w = 377\ \mu$m, and height $h = 157\ \mu$m. (b) The horizontal ultrasound symmetry plane of length $l = 892\ \mu$m and width w in the xy plane at the center of the channel. (c) The vertical channel cross section. The micro-PIV volume around the ultrasound symmetry plane is given as $|z| < 7$ and 47 μm for the 0.6- and 10-μm particles, respectively (see Sec. III C).

Recently, we presented a temperature-controlled microparticle image velocimetry (micro-PIV) setup for accurate measurements of the acoustophoretic microparticle motion in a plane [14]. Here we use the same system and the ability to establish a well-controlled transverse resonance for quantitative studies of how much the radiation- and streaming-induced velocities, respectively, contribute to the total acoustophoretic velocity. More specifically, as illustrated in Fig. 1, we study the microparticle motion in the ultrasound symmetry plane [Fig. 1(b)] of a straight rectangular microchannel of width $w = 377\ \mu$m and height $h = 157\ \mu$m. We determine the velocities for particles of diameter $2a$ ranging from 0.6 to 10 μm, and based on this we examine the validity of Rayleigh's theoretical streaming prediction. We also derive theoretically and validate experimentally an expression for the microparticle velocity as a function of particle size, ultrasound frequency, and mechanical properties of the suspending medium.

II. THEORY OF SINGLE-PARTICLE ACOUSTOPHORESIS

In this work we study a silicon-glass chip containing a rectangular microchannel sketched in Fig. 1 and described further in Sec. III. The microchannel contains a particle suspension and the chip is ultrasonically actuated by attaching a piezo transducer to the chip and driving it with the voltage $U_{\rm pp}$ at the angular frequency $\omega = 2\pi f$, where f is a frequency in the low-MHz range. By proper tuning of the applied frequency, the actuation induces a resonant time-harmonic ultrasonic pressure field $p_1(\boldsymbol{r})\exp(-i\omega t)$ and velocity field $\boldsymbol{v}_1(\boldsymbol{r})\exp(-i\omega t)$, here expressed in the complex time-harmonic notation. In this work we study only the case of a one-dimensional (1D) transverse pressure resonance of amplitude $p_{\rm a}$ and wave number $k = 2\pi/\lambda = n\pi/w$, with integer n,

$$p_1(\boldsymbol{r}) = p_{\rm a}\cos\left[n\pi\left(\frac{y}{w}+\frac{1}{2}\right)\right], \quad n = 1,2,3,\ldots. \tag{1}$$

The case of $\lambda/2 = w$ or $k = \pi/w$ is shown in Fig. 2(a).

The particle suspensions are dilute enough that the particle-particle interactions are negligible and thus only single-particle effects are relevant. These comprise the acoustic radiation force due to particle-wave scattering and the viscous Stokes drag force from the acoustic streaming flow. Both effects are time-averaged second-order effects arising from products of the first-order fields. The drag force from the acoustic streaming flow dominates the motion of small particles, while the motion of larger particles is dominated by the acoustic radiation force. This is clearly illustrated in recent numerical simulations by Muller *et al.* [24], which are reproduced in Fig. 2: The streaming flow advects small particles in a vortex pattern [Fig. 2(b)] and radiation force pushes larger particles to the pressure nodal plane at $y = 0$ [Fig. 2(c)].

A. Acoustic radiation force

We consider a spherical particle of radius a, density $\rho_{\rm p}$, and compressibility $\kappa_{\rm p}$ suspended in a liquid of density ρ_0, compressibility κ_0, viscosity η, and momentum diffusivity $\nu = \eta/\rho_0$. Recently, Settnes and Bruus [22] gave an analytical expression for the viscosity-dependent time-averaged radiation force $\boldsymbol{F}^{\rm rad}$ in the experimentally relevant limit of the wavelength λ being much larger than both the particle radius a and the thickness $\delta = \sqrt{2\nu/\omega}$ of the acoustic boundary layer, without any restrictions on the ratio $\tilde{\delta} = \delta/a$. For the case of a 1D transverse pressure resonance [Eq. (1)], the viscosity-dependent acoustic radiation force on a particle located at (y,z) reduces to the z-independent expression

$$F^{\rm rad}(y,z) = n4\pi^2\Phi(\tilde{\kappa},\tilde{\rho},\tilde{\delta})\frac{a^3E_{\rm ac}}{w}\sin\left(n2\pi\frac{y}{w}+n\pi\right), \tag{2}$$

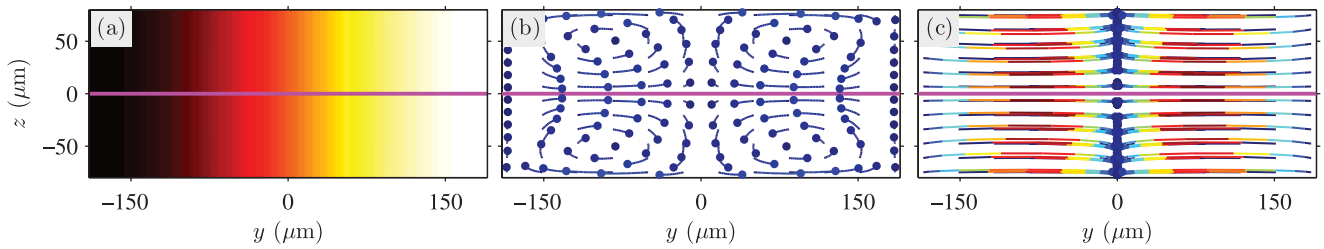

FIG. 2. (Color online) Numerical simulation of microparticle acoustophoresis in the vertical microchannel cross section of Fig. 1(c) adapted from Ref. [24]. The thick horizontal line represents the ultrasound symmetry plane of Fig. 1(b). (a) Color plot of the transverse standing ultrasound pressure wave p_1 of Eq. (1) with $n = 1$ ranging from $-p_{\rm a}$ (black) to $p_{\rm a}$ (white). (b) Trajectories (thin lines) of small 0.5-μm-diam particles (dots) dominated by the Stokes drag force from the boundary-induced streaming. (c) Trajectories (thin colored lines) of large 5.0-μm-diam particles (dots) dominated by the acoustic radiation force.

where $E_{ac} = \frac{1}{4}\kappa_0 p_a^2$ is the time-averaged acoustic energy density and the acoustic contrast factor Φ is given in terms of the material parameters as

$$\Phi(\tilde{\kappa},\tilde{\rho},\tilde{\delta}) = \frac{1}{3}f_1(\tilde{\kappa}) + \frac{1}{2}\mathrm{Re}[f_2(\tilde{\rho},\tilde{\delta})], \tag{3a}$$

$$f_1(\tilde{\kappa}) = 1 - \tilde{\kappa}, \quad \tilde{\kappa} = \frac{\kappa_p}{\kappa_0}, \tag{3b}$$

$$f_2(\tilde{\rho},\tilde{\delta}) = \frac{2[1-\Gamma(\tilde{\delta})](\tilde{\rho}-1)}{2\tilde{\rho}+1-3\Gamma(\tilde{\delta})}, \quad \tilde{\rho} = \frac{\rho_p}{\rho_0}, \tag{3c}$$

$$\Gamma(\tilde{\delta}) = -\frac{3}{2}[1 + i(1+\tilde{\delta})]\tilde{\delta}, \quad \tilde{\delta} = \frac{\delta}{a}. \tag{3d}$$

We note that for all the microparticle suspensions studied in this work including the viscous 0.75:0.25 water:glycerol mixture, the viscous corrections to Φ are negligible as we find $|\Phi(\tilde{\kappa},\tilde{\rho},\tilde{\delta})/\Phi(\tilde{\kappa},\tilde{\rho},0) - 1| < 0.4\%$.

If $\boldsymbol{F}^{rad}$ is the only force acting on a suspended particle, the terminal speed of the particle is ideally given by the Stokes drag as $\boldsymbol{u}^{rad} = \boldsymbol{F}^{rad}/6\pi\eta a$. Using Eq. (2) for the transverse resonance, $\boldsymbol{u}^{rad}$ only has a horizontal component u_y^{rad}, which can be written in the form

$$u_y^{rad} = u_0 \frac{a^2}{a_0^2} \sin\left(n2\pi\frac{y}{w} + n\pi\right), \tag{4}$$

where the characteristic velocity amplitude u_0 and particle radius a_0 are given by

$$u_0 = \frac{4E_{ac}}{\rho_0 c_0} = \frac{4E_{ac}}{Z_0} = 27\ \mu\mathrm{m\,s^{-1}}, \tag{5a}$$

$$a_0 = \sqrt{\frac{6\nu}{\Phi}\frac{1}{\omega}} = \delta\sqrt{\frac{3}{\Phi}} = 1.6\ \mu\mathrm{m}. \tag{5b}$$

Here Z_0 is the characteristic acoustic impedance and the numerical values are calculated for polystyrene particles suspended in water using parameter values listed in Sec. III with $f = 2$ MHz and $E_{ac} = 10\ \mathrm{J\,m^{-3}}$ as in Refs. [15,16].

B. Boundary-driven acoustic streaming

In 1884 Lord Rayleigh [23] published his now classical analysis of the boundary-driven acoustic streaming velocity field $\boldsymbol{U}$ in an infinite parallel-plate channel induced by a first-order bulk velocity field having only a horizontal y component given by $v_1 = v_a \sin[n\pi(y/w + 1/2)]$. This corresponds to the first-order pressure of Eq. (1) illustrated in Fig. 2(a). For an isothermal fluid in the case of $\lambda \gg h \gg \delta$, Rayleigh found the components $U_y(y,z)$ and $U_z(y,z)$ of $\boldsymbol{U}$ outside the acoustic boundary to be

$$U_y = \frac{3}{16}\frac{v_a^2}{c_0}\sin\left(n2\pi\frac{y}{w} + n\pi\right)\left[1 - 3\frac{(2z)^2}{h^2}\right], \tag{6a}$$

$$U_z = \frac{3}{16}\frac{v_a^2}{c_0}\frac{n\pi h}{w}\cos\left(n2\pi\frac{y}{w} + n\pi\right)\left[\frac{(2z)^3}{h^3} - \frac{2z}{h}\right], \tag{6b}$$

$$v_a = \frac{p_a}{\rho_0 c_0} = 2\sqrt{\frac{E_{ac}}{\rho_0}}. \tag{6c}$$

A plot of $\boldsymbol{U}$ driven by the 1D transverse standing half-wave resonance is shown in Fig. 3. We expect this analytical expression to deviate from our measurements because the actual channel does have sidewalls, it is not isothermal, and instead of $\lambda \gg h$ we have $\lambda = 4.8h$ for $\lambda = 2w$ and $\lambda = 2.4h$ for $\lambda = w$.

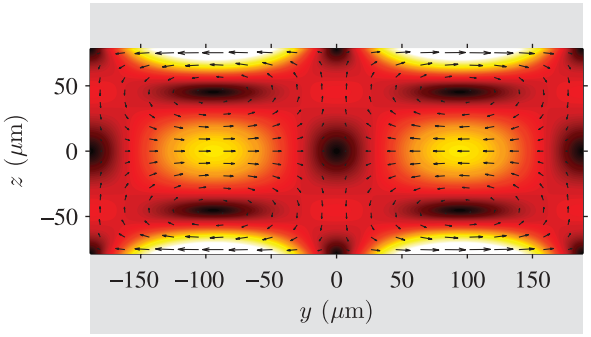

FIG. 3. (Color online) Vector plot (black arrows) of the acoustic streaming $\boldsymbol{U}$ and color plot of its magnitude U from zero (black) to maximum (white) given by Rayleigh's analytical expression [Eqs. (12)] and valid for a shallow isothermal liquid slab ($\lambda \gg h$) between two parallel plates (gray) of distance h driven by a standing ultrasound pressure wave $p_1 = p_a\cos[n\pi(y/w + 1/2)]$ for $n = 1$ and $w = 377\ \mu$m.

At the ultrasound symmetry plane $z = 0$, $\boldsymbol{U}$ only has a horizontal component, which we denote u_y^{str}. In analogy with Eq. (4) this can be written as

$$u_y^{str} = u_0 s_p^0 \sin\left(n2\pi\frac{y}{w} + n\pi\right), \quad s_p^0 = \frac{3}{16} \approx 0.188, \tag{7}$$

where the subscript and superscript in the streaming coefficient s_p^0 refer respectively to the parallel-plate geometry and the isothermal liquid in Rayleigh's analysis.

To estimate the effect on u_y^{str} of the sidewalls and the large height $h \approx \lambda$ in the rectangular channel of Fig. 1(c), we use the numerical scheme developed by Muller *et al.* [24] for calculating the acoustic streaming based directly on the hydrodynamic equations and resolving the acoustic boundary layers, but without taking thermoviscous effects fully into account. The result shown in Fig. 4 reveals that u_y^{str} is suppressed by a factor of 0.82 in the rectangular geometry relative to the parallel-plate geometry and that it approaches zero faster near the sidewalls at $y = \pm w/2$. The approximate

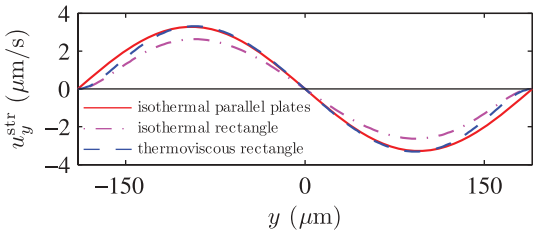

FIG. 4. (Color online) Numerical simulation of the horizontal component u_y^{str} of the streaming velocity in the ultrasound symmetry plane at $z = 0$. In this plane the vertical component is zero $u_z^{str} = 0$. Three cases are shown: the isothermal parallel-plate channel [Eq. (7)], the isothermal rectangular channel [Eq. (8)], and the thermoviscous rectangular channel [Eq. (10)].

result is

$$u_y^{\mathrm{str}} \approx u_0 s_{\mathrm{r}}^0 \sin\left(n2\pi\frac{y}{w} + n\pi\right), \quad s_{\mathrm{r}}^0 \approx 0.154, \tag{8}$$

where the subscript and superscript in the streaming coefficient s_{r}^0 refer respectively to the rectangular geometry and the isothermal liquid.

We estimate the thermoviscous effect on u_y^{str}, in particular the temperature dependence of viscosity, using the analytical result by Rednikov and Sadhal for the parallel-plate geometry [25]. They found a streaming factor s_{p}^T enhanced relative to s_{p}^0,

$$s_{\mathrm{p}}^T = \left(1 + \frac{2}{3}B_T\right)s_{\mathrm{p}}^0 \approx 1.26 s_{\mathrm{p}}^0, \tag{9a}$$

$$B_T = (\gamma - 1)\left[1 - \frac{(\partial_T \eta)_p}{\eta\alpha}\right]\frac{\sqrt{\nu D_{\mathrm{th}}}}{\nu + D_{\mathrm{th}}}, \tag{9b}$$

where α is the thermal expansion coefficient, D_{th} is the thermal diffusivity, γ is the specific heat ratio, and the value is calculated for water at $T = 25\,^{\circ}\mathrm{C}$.

Combining the reduction factor 0.82 from the rectangular geometry with the enhancement factor 1.26 from thermoviscous effects leads to $s_{\mathrm{r}}^T \approx 1.03 s_{\mathrm{p}}^0$ or

$$u_y^{\mathrm{str}} \approx u_0 s_{\mathrm{r}}^T \sin\left(n2\pi\frac{y}{w} + n\pi\right), \quad s_{\mathrm{r}}^T \approx 0.194, \tag{10}$$

where the subscript and superscript in the streaming coefficient s_{r}^T refer respectively to the rectangular geometry and a thermoviscous liquid (see Fig. 4).

C. Acoustophoretic particle velocity

A single particle undergoing acoustophoresis is directly acted upon by the acoustic radiation force $\boldsymbol{F}^{\mathrm{rad}}$, while the acoustic streaming of velocity $\boldsymbol{U}$ contributes with a force on the particle through the viscous Stokes drag from the suspending liquid. Given a maximum acoustophoretic velocity $u^{\mathrm{p}} \approx 1$ mm/s for the largest particles of $a = 5\ \mu$m, the liquid Reynolds number becomes $\rho_0 a^2 u^{\mathrm{p}}/\eta \approx 5 \times 10^{-3}$ and the particle inertia relative to the viscous drag is $[(4/3)\pi a^3 \rho_{\mathrm{p}}(u^{\mathrm{p}}/\tau)]/6\pi\eta a u^{\mathrm{p}} < 6 \times 10^{-3}$ using the observed time scale $\tau > 1$ ms for acceleration of the particles. Consequently, inertial effects can be neglected.

The equation of motion for a spherical particle of velocity $\boldsymbol{u}^{\mathrm{p}}$ then becomes

$$\boldsymbol{u}^{\mathrm{p}} = \frac{\boldsymbol{F}^{\mathrm{rad}}}{6\pi\eta a} + \boldsymbol{U}. \tag{11}$$

As we have seen above, there are no vertical velocity components in the ultrasound symmetry plane at $z = 0$, and combining Eqs. (4) and (10) we obtain the horizontal particle velocity component u_y^{p} of amplitude u_{a},

$$u_y^{\mathrm{p}} = u_y^{\mathrm{rad}} + u_y^{\mathrm{str}} = u_{\mathrm{a}} \sin\left(n2\pi\frac{y}{w} + n\pi\right), \tag{12a}$$

$$u_{\mathrm{a}} = u_0 \frac{a^2}{a_0^2} + u_0 s, \tag{12b}$$

where we have dropped the subscripts and superscripts of the streaming coefficient s. The ratio of the radiation- and streaming-induced velocity amplitudes becomes

$$\frac{u_y^{\mathrm{rad}}}{u_y^{\mathrm{str}}} = \frac{1}{s}\frac{a^2}{a_0^2} = \frac{1}{6s}\frac{\Phi}{\nu}\omega a^2, \tag{13}$$

which scales linearly with the angular frequency ω and the square a^2 of the particle radius, but inversely with the streaming coefficient s and the momentum diffusivity ν/Φ rescaled by the acoustic contrast factor.

In Fig. 5 we show contour plots of the ratio $u_y^{\mathrm{rad}}/u_y^{\mathrm{str}}$ for polystyrene particles in water at 25 °C as function of the particle diameter $2a$ and the ultrasound frequency f [Fig. 5(a)] and

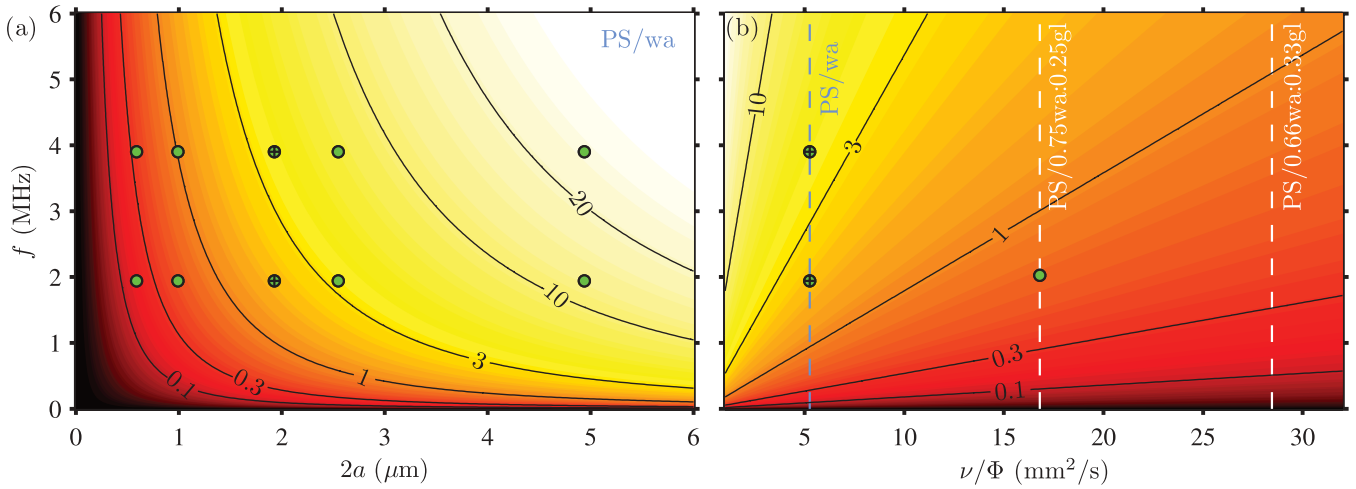

FIG. 5. (Color online) Theoretical prediction of the ratio $u_y^{\mathrm{rad}}/u_y^{\mathrm{str}}$ [Eq. (13)] of radiation- and streaming-induced velocities in the ultrasound symmetry plane of the microchannel [Fig. 1(b) and thick line in Fig. 2] at 25 °C. (a) Contour plot of $u_y^{\mathrm{rad}}/u_y^{\mathrm{str}}$ as a function of particle diameter $2a$ and ultrasound frequency f for a suspension of polystyrene particles (PS) in pure water. (b) Contour plot of $u_y^{\mathrm{rad}}/u_y^{\mathrm{str}}$ as a function of f and the rescaled momentum diffusivity ν/Φ for fixed particle diameter $2a = 2\ \mu$m. The dots indicate the cases studied experimentally in Secs. III and IV. Suspensions of polystyrene particles in three different liquids are indicated by dashed lines: pure water (dark) as well as 0.75:0.25 and 0.67:0.33 mixtures of water:glycerol (white).

as function of f and the rescaled momentum diffusivity ν/Φ for fixed particle diameter $2a = 2\ \mu$m [Fig. 5(b)]. The solid dots indicate the experiments described in Secs. III and IV.

We define the critical particle diameter $2a_c$ for crossover from radiation-dominated to streaming-dominated acoustophoresis as the particle diameter for which $u_y^{\mathrm{rad}}(a_c) = u_y^{\mathrm{str}}(a_c)$. This results in

$$2a_c = 2a_0\sqrt{s} = \sqrt{\frac{24\nu}{\omega}\frac{s}{\Phi}} \approx 1.4\ \mu\mathrm{m}, \tag{14}$$

where the numerical value is calculated for polystyrene particles in water ($\Phi = 0.17$) at $f = 2$ MHz using $s = s_{\mathrm{r}}^{\tilde{T}}$. For $a = a_c$ the ratio of the velocity amplitudes $u_y^{\mathrm{rad}}/u_y^{\mathrm{str}}$ is unity and consequently the unity contour line in Fig. 5(a) represents $2a_c$ as a function of ultrasound frequency f.

D. Wall corrections to single-particle drag

The submillimeter width and height of the rectangular microchannel enhance the hydrodynamic drag on the microparticles. This problem was treated by Faxén for a sphere moving parallel to a planar wall or in between a pair of parallel planar walls [26]. Later, Brenner studied motion perpendicular to a planar wall [27]. (See also the thorough review by Happel and Brenner [28].) The enhancement of the Stokes drag is characterized by a dimensionless correction factor $\chi(a)$ modifying Eqs. (12),

$$u_y^{\mathrm{p}} = \left[\frac{1}{\chi(a)}\frac{a^2}{a_0^2} + s\right]u_0 \sin\left(n2\pi\frac{y}{w} + n\pi\right). \tag{15}$$

No general analytical form exists for χ, so we list the result for three specific cases. For a particle moving parallel to the surface in the symmetry plane $z = 0$ in the gap of height h between two parallel planar walls, χ is

$$\chi_{z=0}^{\mathrm{paral}} \approx [1 - 1.004(2a/h) + 0.418(2a/h)^3]^{-1} \approx 1.070, \tag{16}$$

while for motion in the planes at $z = \pm h/4$ it is

$$\chi_{z=\pm h/4}^{\mathrm{paral}} \approx [1 - 1.305(2a/h) + 1.18(2a/h)^3]^{-1} \approx 1.092. \tag{17}$$

Here the numerical values refer to a particle with diameter $2a = 10\ \mu$m moving in a gap of height $h = 157\ \mu$m. Similarly, for particle motion perpendicular to a single planar wall, the correction factor is

$$\chi^{\mathrm{perp}} = \frac{4}{3}\sinh(\alpha)\sum_{j=1}^{\infty}\frac{j(j+1)}{(2j-1)(2j+3)} \times\left[\frac{2\sinh[(2j+1)\alpha] + (2j+1)\sinh(2\alpha)}{4\sinh^2\left[(j+\frac{1}{2})\alpha\right] - (2j+1)^2\sinh^2(\alpha)} - 1\right] \approx 1.065, \tag{18}$$

where $\alpha = \cosh^{-1}(\Delta y/a)$ and Δy is the distance from the center of the particle to the wall. The numerical value refers to a 10-μm particle located at $\Delta y = w/4$. The values of the wall correction factor χ for all the particle sizes used in this work are summarized in Table I.

TABLE I. Wall correction factor χ to the single-particle drag for the particle sizes used in the experiment.

$2a$ (μm)	$\chi_{z=0}^{\mathrm{paral}}$	$\chi_{z=\pm h/4}^{\mathrm{paral}}$	$\chi_{\Delta y=w/4}^{\mathrm{perp}}$
0.6	1.004	1.005	1.004
1.0	1.006	1.008	1.006
1.9	1.012	1.016	1.011
2.6	1.017	1.022	1.016
4.9	1.032	1.042	1.030
10.2	1.070	1.092	1.065

III. EXPERIMENTAL PROCEDURE

Experiments were carried out to test the validity of the theoretical predictions for the acoustophoretic particle velocity [Eq. (15)] in the horizontal ultrasound symmetry plane and for the ratio of the corresponding radiation and streaming-induced velocities [see Eq. (13) and Fig. 5]. We use the experimental technique and micro-PIV system as presented in Sec. III (Figs. 2 and 3) in Ref. [14]. The setup is automated and temperature controlled. This enables stable and reproducible generation of acoustic resonances as a function of temperature and frequency. It also enables repeated measurements that lead to good statistics in the micro-PIV analyses. The resulting acoustophoretic particle velocities are thus of high precision and accuracy.

Using the chip sketched in Fig. 1, a total of 22 sets of repeated velocity measurement cycles were carried out on polystyrene particles of different diameters undergoing acoustophoresis in different suspending liquids and at different ultrasound frequencies. In the beginning of each measurement cycle, a particle suspension was infused in the channel while flushing out any previous suspensions. Subsequently, the flow was stopped and a time lapse microscope image sequence was recorded at the onset of the ultrasound. The cycle was then repeated.

A. Microparticle suspensions

Two types of microparticle suspensions were examined: polystyrene particles suspended in Milli-Q water and polystyrene particles suspended in a 0.75:0.25 mixture of Milli-Q water and glycerol. Added to each of the two suspending liquids was 0.01% wt./vol Triton-X surfactant to avoid particle adhesion. The material parameters of the suspensions are listed in Table II. Note that the rescaled momentum diffusivity ν/Φ of the glycerol suspension is 3 times larger than that for the Milli-Q water suspension.

We analyzed 12 particle suspensions by adding particles of 6 different diameters $2a$ from 0.6 to 10 μm to the two liquids. The particle diameters were measured by a Coulter Counter (Multisizer 3, Beckman Coulter Inc., Fullerton, CA, USA) and fitting their distributions to Gaussian distributions (see Ref. [35]). The resulting diameters are listed in Table III.

The concentration C of the particles was calculated based on the concentrations provided by the manufacturer and varies in this work from 10^{10} m^{-3} for the largest particles in the 0.75:0.25 mixture of water and glycerol to 10^{15} m^{-3} for the smallest particles in the pure water solution. The

TABLE II. Material parameters at $T = 25\ ^\circ$C. For parameters involving both fluid and solid properties, the solid is always taken to be polystyrene.

Polystyrene		
density[a]	ρ_p	1050 kg m^{-3}
speed of sound[b] (at 20 °C)	c_p	2350 m s^{-1}
Poisson's ratio[c]	σ_p	0.35
compressibility[d]	κ_p	249 T Pa^{-1}
Water		
density[a]	ρ_0	997 kg m^{-3}
speed of sound[a]	c_0	1497 m s^{-1}
viscosity[a]	η	0.890 mPa s
viscous boundary layer, 1.940 MHz	δ	0.38 μm
viscous boundary layer, 3.900 MHz	δ	0.27 μm
compressibility[e]	κ_0	448 T Pa^{-1}
compressibility factor	f_1	0.444
density factor	f_2	0.034
contrast factor	Φ	0.17
rescaled momentum diffusivity	ν/Φ	5.25 mm^{2}s^{-1}
0.75:0.25 mixture of water and glycerol		
density[f]	ρ_0	1063 kg m^{-3}
speed of sound[g]	c_0	1611 m s^{-1}
viscosity[f]	η	1.787 mPa s
viscous boundary layer, 2.027 MHz	δ	0.51 μm
compressibility[e]	κ_0	363 T Pa^{-1}
compressibility factor	f_1	0.313
density factor	f_2	−0.008
contrast factor	Φ	0.10
rescaled momentum diffusivity	ν/Φ	16.8 mm^2 s^{-1}

[a]Reference [29].
[b]Reference [30].
[c]Reference [31].
[d]Calculated as $\kappa_p = \frac{3(1-\sigma_p)}{1+\sigma_p}\frac{1}{\rho_p c_p^2}$ from Ref. [32].
[e]Calculated as $\kappa_0 = 1/\rho_0 c_0^2$.
[f]Reference [33].
[g]Reference [34].

concentrations correspond to mean interparticle distances $C^{-1/3}$ ranging from 4 particle diameters for the largest 10-μm particle in water to 173 particle diameters for the smallest 0.6-μm particle in the 0.75:0.25 mixture of water and glycerol. For this size and concentration range Batchelor's correction factor of $1 - [1.83 \times (4\pi/3)a^3 C]$ for the hydrodynamic effects can be used [36], resulting in negligible quantitative changes less than 0.02%. Mikkelsen and Bruus [37] have reported that the hydrodynamic effects result in qualitative changes for interparticle distances below 2 particle diameters. Thus we can apply the single-particle theory presented in Sec. II.

TABLE III. Nominal and measured diameters of the polystyrene particles used in the experiment.

Nominal diameter	Measured diameter $2a$
591 nm	(0.59 ± 0.03) μm[a]
992 nm	(0.99 ± 0.05) μm[a]
2.0 μm	(1.91 ± 0.07) μm[b]
3.0 μm	(2.57 ± 0.07) μm[b]
5 μm	(5.11 ± 0.16) μm[b]
10 μm	(10.16 ± 0.20) μm[b]

[a]Value from manufacturer and assumed 5% standard deviation.
[b]Measured by the Coulter counter.

B. Measurement series

We measured the acoustophoretic velocities of polystyrene microparticles in the following four series of experiments, the second being a repeat of the first.

MQ0: Milli-Q water, $f = 1.940$ MHz, $\lambda = 2w$, and $2a = 1.0$, 1.9, 2.6, and 5.1 μm.

MQ1: Milli-Q water, $f = 1.940$ MHz, $\lambda = 2w$, and $2a = 0.6$, 1.0, 1.9, 2.6, 5.1, and 10.2 μm.

MQ2: Milli-Q water, $f = 3.900$ MHz $\lambda = w$, and $2a = 0.6$, 1.0, 1.9, 2.6, 5.1, and 10.2 μm.

Gl1: 0.75:0.25 Milli-Q water:glycerol, $f = 2.027$ MHz $\lambda = 2w$, and $2a = 0.6$, 1.0, 1.9, 2.6, 5.1, and 10.2 μm.

Given the different particle diameters, we thus have the above-mentioned 22 sets of acoustophoretic particle-velocity measurements, each consisting of 50–250 measurement cycles. All experiments were carried out at a fixed temperature of 25 °C and the applied piezo voltage U_{pp}^*. The camera frame rate was chosen such that the particles would move at least a particle diameter between two consecutive images. The measurement field of view was 1280×640 pixels corresponding to 892×446 μm^2. The imaging parameters were an optical wavelength of 520 nm for which the microscope objective is most sensitive, a numerical aperture of 0.4, and a magnification of 20. See more details in Ref. [35].

C. Micro-PIV analysis

The micro-PIV analyses were carried out using the software EDPIV—Evaluation Software for Digital Particle Image Velocimetry, including the image procedure, the averaging in correlation space, and the window shifting described in detail in Ref. [14]. For the MQ1, MQ2, and Gl1 series, the interrogation window size was 32×32 pixels with a 50% overlap resulting in a 79×39 square grid with 16 pixels between each grid point. For the MQ0 series, the interrogation window size was 64×64 pixels with a 50% overlap resulting in a 39×19 square grid with 32 pixels between each grid point.

In micro-PIV all particles in the volume are illuminated and the thickness of the measurement plane is therefore related to the focal depth of the microscope objective. This thickness, called the depth of correlation (DOC), is defined as twice the distance from the measurement plane to the nearest plane for which the particles are sufficiently defocused such that it no longer contributes significantly to the cross-correlation analysis [38]. The first analytical expression for the DOC was derived by Olsen and Adrian [39] and later improved by Rossi *et al.* [40]. Using the latter, we found that the DOC ranges from 14 to 94 μm $\approx h/2$ for the smallest and the largest particles, respectively. Consequently, in the vertical direction all observed particles reside within the middle half of the channel.

IV. RESULTS

The core of our results is the 22 discrete acoustophoretic particle-velocity fields obtained by micro-PIV analysis of the 22 sets of acoustic focusing experiments and shown in Ref. [35]. As in Ref. [14], the measured microparticle velocities $\boldsymbol{u}^{\mathrm{p}}$ are thus represented on a discrete $x_n \times y_m$ micro-PIV grid

$$\boldsymbol{u}^{\mathrm{p}} = \boldsymbol{u}^{\mathrm{p}}(x_n, y_m) = \begin{bmatrix} u_x^{\mathrm{p}}(x_n, y_m) \\ u_y^{\mathrm{p}}(x_n, y_m) \end{bmatrix}. \tag{19}$$

All measured velocities presented in the following are normalized to their values at $U_{\mathrm{pp}} = 1$ V using the voltage-squared law [15]

$$\boldsymbol{u}^{\mathrm{p}} = \left(\frac{1\ \mathrm{V}}{U_{\mathrm{pp}}^*}\right)^2 \boldsymbol{u}^{\mathrm{p}*}, \tag{20}$$

where the asterisk denotes the actual measured values. As a result, the extracted velocity amplitudes and acoustic energy densities are normalized as well,

$$u_{\mathrm{a}} = \left(\frac{1\ \mathrm{V}}{U_{\mathrm{pp}}^*}\right)^2 u_{\mathrm{a}}^*, \tag{21a}$$

$$E_{\mathrm{ac}} = \left(\frac{1\ \mathrm{V}}{U_{\mathrm{pp}}^*}\right)^2 E_{\mathrm{ac}}^*. \tag{21b}$$

The actual peak-to-peak values of the applied voltage U_{pp}^* for all four experimental series are given in Ref. [35].

A. Excitation of a 1D transverse standing wave

In Figs. 6 and 7 we verify experimentally that the acoustophoretic particle velocity is of the predicted sinusoidal form given in Eqs. (12) and resulting from a 1D transverse standing wave. For the actual applied voltage of $U_{\mathrm{pp}}^* = 7.94$ V the maximum velocity was measured to be $1.77\ \mathrm{mm\,s^{-1}}$, which by Eq. (20) is normalized to the maximum velocity $u_{\mathrm{max}}^{\mathrm{p}*} = 28\ \mu\mathrm{m\,s^{-1}}$ seen in Fig. 6.

A detailed analysis of the measured velocity field reveals three main points: (i) The average of the ratio of the axial to the transverse velocity component is practically zero $\langle |u_x^{\mathrm{p}}/u_y^{\mathrm{p}}| \rangle < 5\%$, (ii) the maximum particle velocity along any line with a given axial grid point coordinate x_m varies less than 6% as a function of x_m, and (iii) the axial average $\langle u_y^{\mathrm{p}} \rangle_x$ of the transverse velocity component u_y^{p} is well fitted within small error bars ($< 1\%$) by Eqs. (12).

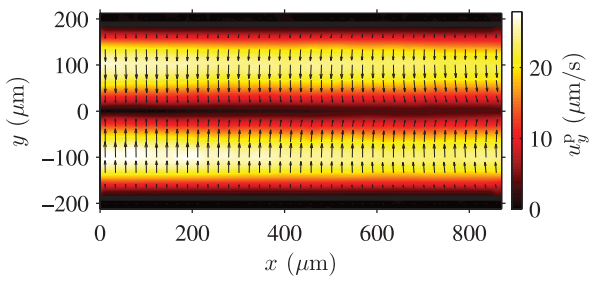

FIG. 6. (Color online) Experimental micro-PIV measurement of acoustophoresis in the horizontal ultrasound symmetry plane of 1-μm-diam polystyrene particles suspended in water and driven at the piezo frequency $f = 1.940$ MHz corresponding to $\lambda/2 = w$, temperature 25 °C, and voltage $U_{\mathrm{pp}}^* = 7.94$ V. The arrows represent the measured velocity vectors $\boldsymbol{u}^{\mathrm{p}}$ and the grayscale (colorscale) their magnitude u^{p} normalized to U_{pp}^* [see Eq. (20)].

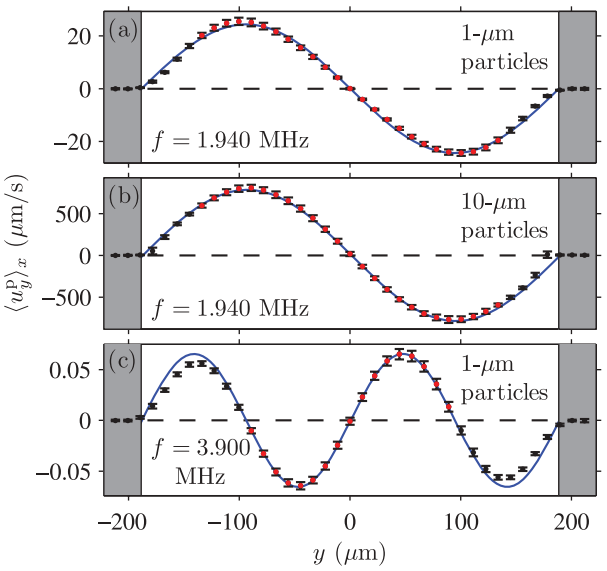

FIG. 7. (Color online) Measured average $\langle u_y^{\mathrm{p}} \rangle_x$ (dark and light points) and its standard deviation $\sigma(\langle u_y^{\mathrm{p}} \rangle_x)$ (error bars) of the transverse velocity u_y^{p} of polystyrene particles in water. The sinusoidal prediction [Eqs. (12)] for u^{p} (solid line) is fitted to data points $\langle u_y^{\mathrm{p}} \rangle_x$ away from the sidewalls (light points). (a) Streaming-dominated acoustophoresis for $2a = 1$ μm driven at $f = 1.940$ MHz ($\lambda/2 = w$, same data as in Fig. 6). (b) Radiation-dominated acoustophoresis for $2a = 10$ μm at $f = 1.940$ MHz ($\lambda/2 = w$). (c) Streaming-dominated acoustophoresis for $2a = 1$ μm at $f = 3.900$ MHz ($\lambda = w$).

B. Measuring the velocity amplitude

In Fig. 7(a) we plot the axial average $\langle u_y^{\mathrm{p}} \rangle_x$ of the transverse velocity component u_y^{p} (dark and light points) and its standard deviation $\sigma(\langle u_y^{\mathrm{p}} \rangle_x)$ (error bars) for the velocity field shown in Fig. 6 at the standing-half-wave resonance frequency $f = 1.940$ MHz for the 1-μm-diam streaming-dominated particles (series MQ1). The measured velocities away from the sidewalls (light points) are fitted well by the predicted sinusoidal velocity profile $u_{\mathrm{a}} \sin(n2\pi y/w + n\pi)$ (solid line) [Eqs. (12)] for fixed wavelength $\lambda = 2w$ and using u_{a} as the only fitting parameter. Velocities close to the sidewalls (black points) are discarded due to their interaction with the sidewalls. As seen numerically in Fig. 4, the no-slip boundary condition on the sidewalls of the rectangular geometry suppresses the streaming velocity near the sidewalls relative to sinusoidal velocity profile of the parallel-plate geometry.

As shown in Fig. 7(b), the theoretical prediction also fits well the measured velocities away from the sidewalls for the large radiation-dominated 10-μm-diam particles (series MQ1, $\lambda/2 = w$). Likewise, as seen in Fig. 7(c), a good fit is also obtained for the 1-μm-diam particles away from the sidewalls at the standing-full-wave frequency $f = 3.900$ MHz (series MQ2, $\lambda = w$). Given this strong support for the presence of standing transverse waves, we use this standing-wave

fitting procedure to determine the velocity amplitude u_a in the following analysis of the acoustophoretic particle velocity.

In spite of the normalization to the same driving voltage of 1 V, the velocity amplitude of the half-wave resonance in Fig. 7(a) is 400 times larger than that of the full-wave resonance in Fig. 7(c). This is due to the different coupling of the piezo transducer to the specific spatial wave structure of each resonance mode and the different dissipation or Q values of these modes.

C. Velocity as a function of particle diameter

To analyze in detail the transverse velocity amplitude u_a in all four series MQ0, MQ1, MQ2, and Gl1, we return to the wall-enhanced drag coefficient χ of Sec. II D. In general, χ depends in a nonlinear way on the motion and position of the particle relative to the rigid walls. However, in Sec. III C we established that the majority of the observed particles reside in the middle half of the channel, and in our standing-wave fitting procedure for u_a in Sec. IV B we discarded particles close to the sidewalls. Consequently, given this and the values of χ in Table I, it is a good approximation to assume that all involved particles have the same wall correction factor, namely, the symmetry-plane parallel-motion factor

$$\chi \approx \chi_{z=0}^{\text{paral}}. \tag{22}$$

As the drag correction only enters on the radiation-induced term in Eq. (15), we introduce a wall-drag-corrected particle size $a_{\text{wd}} = (\chi_{z=0}^{\text{paral}})^{-1/2}\, a$.

To determine the acoustic energy density E_{ac} and the streaming coefficient s we plot in Fig. 8, for each of the four experiment series, u_a/u_0 versus the particle diameter $2a$ (colored symbols) and wall-drag-corrected particle diameter $2a_{\text{wd}}$ (gray symbols). The characteristic velocity amplitude u_0 is determined in each series by fitting the wall-drag-corrected data points to Eqs. (12) using E_{ac} and s as fitting parameters. In all four experiment series, a clear a^2 dependence is seen. Notice further that the velocities follow almost the same distribution around the fitted line in all series. This we suspect may be due to systematic errors, e.g., that the 5-μm-diam particles are slightly underestimated (see the Coulter data in Ref. [35]). The resulting fitting parameters E_{ac} and s are listed in Table IV(a). The energy densities normalized to $U_{\text{pp}} = 1$ V [see Eq. (21b)] vary with more than a factor of 700 due to a large difference in the strength of the excited resonances. According to the predictions in Sec. II, the streaming coefficient s should be constant, but experimentally it varies from 0.18 to 0.26. However, taking the fitting uncertainties into account in a weighted average leads to $\langle s \rangle_w = 0.192 \pm 0.010$, which is close to $s_{\text{r}}^T \approx 0.194$ of Eq. (10).

Another approach for extracting E_{ac} and s is to assume that the smallest particles $2a = 0.6$ μm are influenced only by the streaming-induced drag. If so, the velocity of the largest $2a = 10$ μm particle has a streaming component of less than 6% (see the measured ratios $u_a^{0.6\ \mu\text{m}}/u_a^{10\ \mu\text{m}}$ in Table V). Therefore, we further assume that the 10-μm-diam particles are influenced solely by the radiation force, and from $u_a^{\text{rad}} = u_0(a/a_0)^2$ we

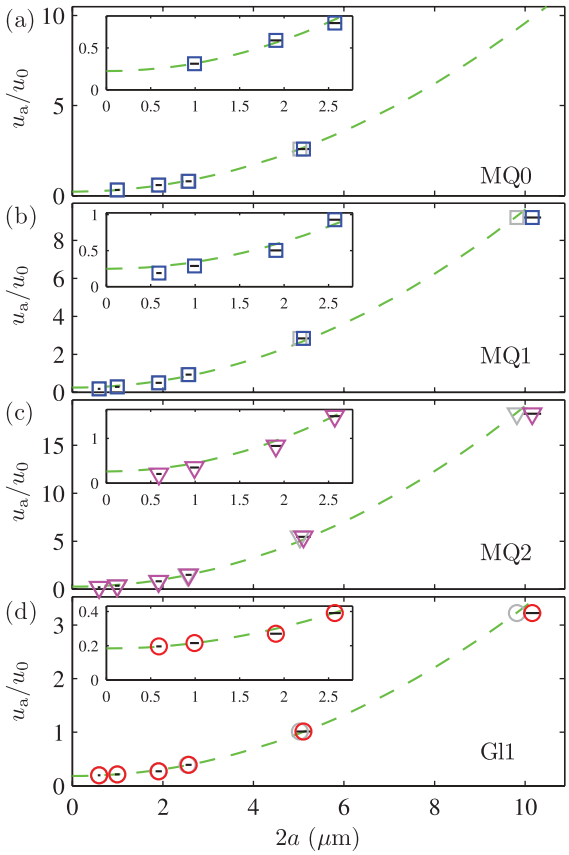

FIG. 8. (Color online) Measured and normalized acoustophoretic velocity amplitudes u_a/u_0 as functions of particle diameter $2a$ (dark colored symbols) and wall-drag-corrected particle diameter $2a_{\text{wd}}$ (light gray symbols) for the four experiment series (a) MQ0, (b) MQ1, (c) MQ2, and (d) Gl1 described in Sec. III B. The characteristic velocity amplitude u_0 is determined from fitting Eqs. to the gray points in each series using E_{ac} and s as fitting parameters resulting in the values listed in Table IV(a) (green dashed lines). The standard deviation of u_a/u_0 is less than the symbol size and the standard deviations on the particle diameters are indicated as black lines.

determine the acoustic energy density as

$$E_{\text{ac}} = \frac{3}{2}\frac{\eta c_0}{\Phi\omega}\frac{u_a^{10\ \mu\text{m}}}{a_{\text{wd}}^2}. \tag{23}$$

Knowing the acoustic energy density, we use Eq. (7) to calculate the streaming coefficient s from $u_a^{\text{str}} = u_0 s$ as

$$s = \frac{\rho_0 c_0}{4E_{\text{ac}}} u_a^{0.6\ \mu\text{m}}. \tag{24}$$

Assuming that the largest error is due to the dispersion in particle size, we obtain the results listed in Table IV(b). The acoustic energy densities are close to the ones extracted from the fits in Fig. 8 and the geometric streaming coefficient varies from 0.180 to 0.203 with an weighted average of $\langle s \rangle_w = 0.191 \pm 0.005$. Note that using Eqs. (23) and (24), we only need to consider the dispersion of the 10-μm-diam particles, which results in a more reliable estimate of s.

We use the acoustic energy densities in Table IV(b) together with the material parameters in Table II to calculate u_0 and a_0 [Eqs. (5)] for each of the experiment series MQ1, MQ2, and

TABLE IV. Measured acoustic energy densities E_{ac} normalized to $U_{pp} = 1$ V and streaming coefficient s.

(a) Unweighted fit to all points (see Fig. 8)

Suspension	Frequency (MHz)	E_{ac} (J m^{-3})	s
MQ0	1.940	52.306 ± 0.918	0.222 ± 0.025
MQ1	1.940	31.807 ± 0.569	0.247 ± 0.071
MQ2	3.900	0.070 ± 0.001	0.262 ± 0.125
Gl1	2.027	2.420 ± 0.020	0.184 ± 0.012

(b) Based on particles with $2a = 0.6$ and 10 μm

Suspension	Frequency (MHz)	E_{ac} (J m^{-3})[a]	s[b]
MQ1	1.940	32.436 ± 1.282	0.182 ± 0.008
MQ2	3.900	0.071 ± 0.003	0.205 ± 0.008
Gl1	2.027	2.559 ± 0.110	0.186 ± 0.008

[a]Equation (23).
[b]Equation (24).

Gl1. According to the theoretical prediction in Eqs. (12), all data points must fall on a straight line of unity slope and intersection s if plotted as the normalized velocity amplitude u_a/u_0 as function of the normalized particle radius squared $(a/a_0)^2$. The plot is shown in Fig. 9, showing good agreement with the theoretical prediction using $s_r^T \approx 0.194$.

D. Velocity ratios

In Table V we list velocity ratios for different particle sizes in the experiment series MQ1, MQ2, and Gl1. From Eqs. (12) we expect $u_a - u_a^{str} \propto a^2$, leading to the prediction $(u_a^{5\,\mu m} - u_a^{str})/(u_a^{10\,\mu m} - u_a^{str}) = (5/10)^2 = 0.25$. If we assume that the smallest 0.6-μm-diam particles are only influenced by the acoustic streaming, we have $u_a^{str} = u_a^{0.6\,\mu m}$. We can therefore test the just-mentioned hypothesis by calculating $(u_a^{5\,\mu m} - u_a^{0.6\,\mu m})/(u_a^{10\,\mu m} - u_a^{0.6\,\mu m})$. The results are listed in the fifth column in Table V, where we obtain values ranging from 0.27 to 0.29, or a deviation of 8–18%.

Assuming that the smallest 0.6-μm-diam particles and the largest 10-μm-diam particles are influenced only by the acoustic streaming and the acoustic radiation force, respectively, we can estimate the ratio of radiation- and streaming-induced velocities as $u_a^{rad}/u_a^{str} = u_a^{10\,\mu m}/u_a^{0.6\,\mu m}$, which are listed in the fourth column in Table V. First, we notice that the ratio increases by a factor of $88.4/49.6 = 1.8$ as we increase the frequency by a factor of $3.900/1.940 = 2.0$. This agrees well with a linear increase with frequency as predicted by Eq. (13). Second, we notice that the ratio increases by a factor of $48.6/16.4 = 3.0$ as we change the suspending medium from a 0.75:0.25 mixture of water and glycerol to pure water. According to Eq. (13), u_a^{rad}/u_a^{str} increases linearly with ν/Φ and from Table II we obtain a predicted ratio increase of $16.8/5.25 =$ 3.2, which matches well with the experimentally estimated ratio. With these results we have gained experimental support for the theoretical prediction of the velocity ratio given in Eq. (13).

TABLE V. Relative particle velocities.

Suspension	Frequency (MHz)	$\frac{u_a^{0.6\,\mu m}}{u_a^{10\,\mu m}}$	$\frac{u_a^{10\,\mu m}}{u_a^{0.6\,\mu m}}$	$\frac{u_a^{5\,\mu m} - u_a^{0.6\,\mu m}}{u_a^{10\,\mu m} - u_a^{0.6\,\mu m}}$
MQ1	1.940	0.020	49.6	0.294
MQ2	3.900	0.011	88.4	0.291
Gl1	2.027	0.061	16.4	0.270

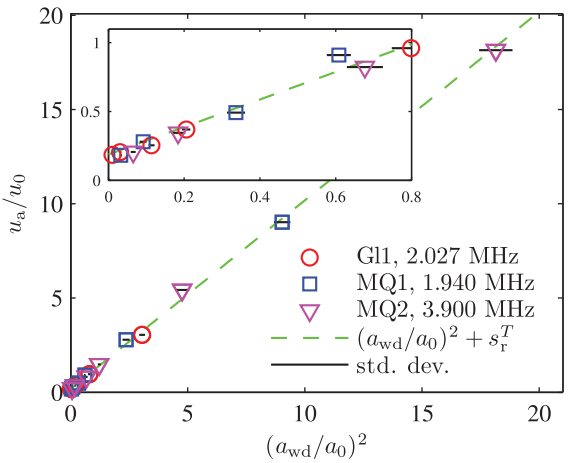

FIG. 9. (Color online) Plot of the measured normalized acoustophoretic particle velocity amplitude u_a/u_0 versus the square $(a_{wd}/a_0)^2$ of the normalized wall-drag-corrected particle radius. The dashed line is a fit to Eqs. (12).

V. DISCUSSION

Our results verify experimentally the theoretically predicted dependence of the magnitude of the acoustophoretic velocity in a microchannel on the viscosity of the suspending liquid, the acoustic contrast factor Φ, and the ultrasound frequency. For most situations involving cells, isotonic solutions are used such as phosphate-buffered saline, sodium chloride, or blood plasma. Direct manipulation of small particles such as bacteria in plasma or in buffers of high levels of protein is problematic, primarily due to the high viscosity of those media. When possible, these media should be exchanged prior to manipulation to increase the potential for success.

Increasing the frequency in the system would allow for a reduction of the critical diameter of particles. One adverse effect of a higher frequency is that the channel width must be narrowed down, which affects the throughput in the system. This problem can, however, be overcome by designing a channel of high aspect ratio, where the resonance occurs over the smallest dimension [41].

Another benefit of high-aspect-ratio channels was pointed out by Muller *et al.* [24]. Since the acoustic streaming emanates from the walls perpendicular to the wave propagation (here the top and bottom), a high channel leads to a weaker average streaming field in the center.

The measurements of particle velocities for polystyrene particles ranging from 0.6 to 10 μm give no support to previous measurements presented by Yasuda and Kamakura [42]. Their rather spectacular result was that particles below a certain size move faster than larger particles do. From the experiments reported herein it is clear, however, that the motion of particles indeed can be well described with the analyses presented by Rayleigh [23], Yosioka and Kawasima [17], and Gorkov [18].

The uncertainties in the measured particle velocities may in particular be due to the following four causes: (i) variations in particle density ρ_p and compressibility κ_p as a function of particle producer (Fluka and G. Kisker) or batch, (ii) deviations from normal distributed particle sizes as shown in Fig. 1 of Ref. [35], (iii) local fluctuations in the bead concentrations leading to particle-particle interactions, and (iv) viscosity variations induced by the suspended particles.

To better understand the nature of acoustic streaming in microchannels the streaming field should be mapped for the channel cross section and along the whole length of the channel. As reported by Hagsäter *et al.* [43] and Augustsson *et al.* [14], the acoustic field can deviate dramatically from the very uniform one-dimensional field reported herein. Nonsymmetrical acoustic fields can be expected to generate far more complex streaming fields.

VI. CONCLUSION

We have investigated the motion of microparticles due to acoustic radiation and acoustic streaming inside a liquid-filled long, straight rectangular channel of width w and height h driven by an ultrasound standing wave of wavelength λ. Fortuitously, the simple analytical expression derived by Lord Rayleigh for the streaming velocity in an isothermal liquid slab between two infinite parallel plates fulfilling $\lambda \gg h$ is a good approximation for the specific rectangular channel of Fig. 1 containing a thermoviscous liquid and fulfilling $\lambda \approx h$. The reduction in velocity obtained when replacing the parallel plates with the rectangular geometry is almost perfectly compensated for by the enhancement in velocity from replacing the isothermal liquid by the thermoviscous one.

A theoretical prediction was made [Eqs. (12)] for the dependence of the radiation- and streaming-induced velocities on the size of the particles, the ultrasound frequency, the viscosity of the suspending liquid, and the acoustic contrast factor. This prediction was found to be in excellent agreement with experimental findings as shown by the collapse after re-scaling of data from 22 different measurements on the same line in Fig. 9. The results have bearing on acoustophoretic manipulation strategies for submicrometer biological particles such as bacteria and vira, which are too small to be handled using the present manifestation of this technique. We can conclude that increasing the ultrasound frequency, increasing the channel aspect ratio, and lowering the viscosity of the suspending fluid is probably the most viable route to conduct such manipulation.

ACKNOWLEDGMENTS

This research was supported by the Danish Council for Independent Research, Technology and Production Sciences, Grant No. 274-09-0342; the Swedish Research Council, Grant No. 2007-4946; and the Swedish Governmental Agency for Innovation Systems, VINNOVA, the program Innovations for Future Health, Cell CARE, Grant No. 2009-00236.

[1] J. Friend and L. Y. Yeo, Rev. Mod. Phys. **83**, 647 (2011).
[2] H. Bruus, J. Dual, J. Hawkes, M. Hill, T. Laurell, J. Nilsson, S. Radel, S. Sadhal, and M. Wiklund, Lab Chip **11**, 3579 (2011).
[3] J. J. Hawkes, R. W. Barber, D. R. Emerson, and W. T. Coakley, Lab Chip **4**, 446 (2004).
[4] F. Petersson, A. Nilsson, C. Holm, H. Jönsson, and T. Laurell, Analyst **129**, 938 (2004).
[5] P. Thevoz, J. D. Adams, H. Shea, H. Bruus, and H. T. Soh, Anal. Chem. **82**, 3094 (2010).
[6] P. Augustsson, C. Magnusson, M. Nordin, H. Lilja, and T. Laurell, Anal. Chem. **84**, 7954 (2012).
[7] X. Ding, S.-C. S. Lin, B. Kiraly, H. Yue, S. Li, I.-K. Chiang, J. Shi, S. J. Benkovic, and T. J. Huang, Proc. Natl. Acad. Sci. USA **109**, 11105 (2012).
[8] B. Vanherberghen, O. Manneberg, A. Christakou, T. Frisk, M. Ohlin, H. M. Hertz, B. Önfelt, and M. Wiklund, Lab Chip **10**, 2727 (2010).
[9] P. Augustsson and T. Laurell, Lab Chip **12**, 1742 (2012).
[10] M. Bengtsson and T. Laurell, Anal. Bioanal. Chem. **378**, 1716 (2004).
[11] L. A. Kuznetsova, S. P. Martin, and W. T. Coakley, Biosens. Bioelectron. **21**, 940 (2005).
[12] S. P. Martin, R. J. Towsend, L. A. Kuznetsova, K. A. J. Borthwick, M. Hill, M. B. McDonnell, and W. T. Coakley, Biosens Bioelectron **21**, 758 (2005).
[13] B. Hammarström, T. Laurell, and J. Nilsson, Lab Chip **12**, 4296 (2012).
[14] P. Augustsson, R. Barnkob, S. T. Wereley, H. Bruus, and T. Laurell, Lab Chip **11**, 4152 (2011).
[15] R. Barnkob, P. Augustsson, T. Laurell, and H. Bruus, Lab Chip **10**, 563 (2010).
[16] R. Barnkob, I. Iranmanesh, M. Wiklund, and H. Bruus, Lab Chip **12**, 2337 (2012).
[17] K. Yosioka and Y. Kawasima, Acustica **5**, 167 (1955).
[18] L. P. Gorkov, Sov. Phys.—Dokl. **6**, 773 (1962).
[19] M. Wiklund, R. Green, and M. Ohlin, Lab Chip **12**, 2438 (2012).
[20] J. F. Spengler, W. T. Coakley, and K. T. Christensen, AIChE J. **49**, 2773 (2003).
[21] S. M. Hagsäter, T. G. Jensen, H. Bruus, and J. P. Kutter, Lab Chip **7**, 1336 (2007).
[22] M. Settnes and H. Bruus, Phys. Rev. E **85**, 016327 (2012).
[23] L. Rayleigh, Philos. Trans. R. Soc. London **175**, 1 (1884).
[24] P. B. Muller, R. Barnkob, M. J. H. Jensen, and H. Bruus, Lab Chip **12**, 4617 (2012).
[25] A. Y. Rednikov and S. S. Sadhal, J. Fluid Mech. **667**, 426 (2011).
[26] H. Faxén, Ann. Phys. **68**, 89 (1922).
[27] H. Brenner, Chem. Eng. Sci. **16**, 242 (1961).
[28] J. Happel and H. Brenner, *Low Reynolds Number Hydrodynamics with Special Applications to Particulate Media* (Nijhoff Publishers, The Hague, 1983).
[29] *CRC Handbook of Chemistry and Physics*, 92nd ed. (Taylor and Francis, London, 2012), www.hbcpnetbase.com/.

[30] L. Bergmann, *Der Ultraschall und seine Anwendung in Wissenschaft und Technik*, 6th ed. (Hirzel, Stuttgart, 1954).
[31] P. H. Mott, J. R. Dorgan, and C. M. Roland, J. Sound. Vibr. **312**, 572 (2008).
[32] L. D. Landau and E. M. Lifshitz, *Theory of Elasticity. Course of Theoretical Physics*, 3rd ed. (Pergamon, Oxford, 1986), Vol. 7.
[33] N.-S. Cheng, Ind. Eng. Chem. Res. **47**, 3285 (2008).
[34] F. Fergusson, E. Guptill, and A. MacDonald, J. Acoust. Soc. Am. **26**, 67 (1954).
[35] See Supplemental Material at http://link.aps.org/supplemental/10.1103/PhysRevE.86.056307 for more details regarding the Coulter counter data, the acquisition table of logged experimental data, and all measured acoustophoretic velocity fields.
[36] G. K. Batchelor, J. Fluid Mech. **74**, 1 (1976).
[37] C. Mikkelsen and H. Bruus, Lab Chip **5**, 1293 (2005).
[38] C. Meinhart, S. Wereley, and M. Gray, Meas. Sci. Technol. **11**, 809 (2000).
[39] M. G. Olsen and R. J. Adrian, Exp. Fluids Suppl. **29**, S166 (2000).
[40] M. Rossi, R. Segura, C. Cierpka, and C. J. Kähler, Exp. Fluids **52**, 1063 (2012).
[41] J. D. Adams, C. L. Ebbesen, R. Barnkob, A. H. J. Yang, H. T. Soh, and H. Bruus, J. Micromech. Microeng. **22**, 075017 (2012).
[42] K. Yasuda and T. Kamakura, Appl. Phys. Lett. **71**, 1771 (1997).
[43] S. M. Hagsäter, A. Lenshof, P. Skafte-Pedersen, J. P. Kutter, T. Laurell, and H. Bruus, Lab Chip **8**, 1178 (2008).